ACS Sustainable Chemistry & Engineering

pubs.acs.org/journal/ascecg

Research Article

Eco-Friendly Bionic Flexible Multifunctional Sensors Based on Biomass−MXene Composites

Chi Zheng, Dangge Gao,* Bin Lyu, Yingying Zhou, Ailin Zhang, Yu Gu, Jianzhong Ma,* Davida Briana DuBois, and Shaowei Chen*

Cite This: *ACS Sustainable Chem. Eng.* 2023, 11, 5834−5844

Read Online

ACCESS | Metrics & More | Article Recommendations | Supporting Information

ABSTRACT: Flexible sensors with multifunctions have attracted great attention for their extensive application values. Most of the reported multifunctional flexible sensors lack the intuitive signal display function, have limitations of work environment, and are weakly resistant to electromagnetic waves, and the landfill and incineration of the sensor wastes could pose irreversible damage to the environment. Herein, a trilayer composite (referred to as TGM) is prepared by the layer-by-layer assembly of MXene, gelatin, and a water-based multiporous membrane (WMM), which exhibits a hierarchically ordered bionic heterostructure. The top layer is multilayers of MXene nanosheets, the middle layer consists of artificial neural cages and synapses from an MXene@gelatin structure, and the bottom layer is a brick-mortar mimic of MXene@WMM. The resulting TGM heterostructure displays excellent performance in pressure sensing both in air and under water due to the ready variation of the electrical conductivity with applied pressures. The TGM composite also shows an apparent actuation response under IR, moisture, and heating stimulations. These multifunctional characteristics can be integrated for visual sensing of environmental temperature and humidity. Additionally, the composite possesses efficient electromagnetic shielding and shows great degradation. Results from this study highlight the unique potential of MXene−biomass composites in the development of eco-friendly multifunctional sensors.

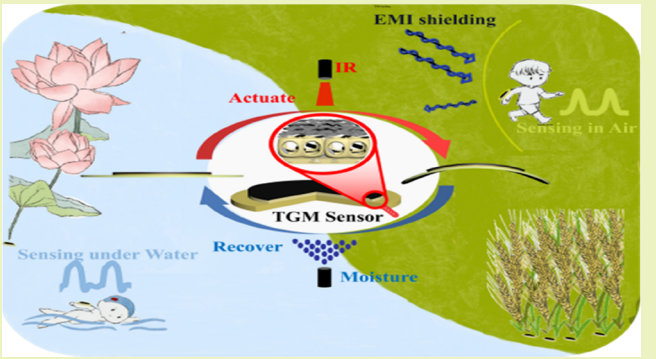

KEYWORDS: *$Ti_3C_2T_x$ MXene, gelatin, bionic structure, sensing, actuating, electromagnetic shielding, eco-friendly*

INTRODUCTION

Smart flexible sensors have found diverse applications in, for instance, medical diagnostics and therapy, bionic intelligent robotics, and human−computer interactions.[1−3] Among these, multifunctional smart and interactive electronic sensors are of particular interest,[4,5] where the selection of an appropriate substrate is critical in endowing the flexible sensors with various functions, such as poly(vinyl alcohol) for self-healing,[6] poly(dimethylsiloxane) for self-cleaning,[7] and luminous thermoplastic urethane for visualization sensing.[8] Such substrates can be divided into two categories, synthetic polymers and natural biomass. The latter has been attracting extensive interest because of their biocompatibility and biodegradability. For instance, gelatin has been used in flexible sensors due to its abundant functional groups, unique triple-helix structure, and low cost.[9,10] In addition, the sensing performance can be further enhanced by the structural engineering of the gelatin.[11,12]

In recent years, a range of multifunctional flexible sensors have been developed based on $Ti_3C_2T_x$ MXene.[13,14] Yet, as $Ti_3C_2T_x$ MXene is prone to oxidation, the development of such sensor technologies is greatly hampered.[15] This issue can be mitigated by encapsulating $Ti_3C_2T_x$ MXene within polymeric materials to minimize contact with oxygen and water, such as polydopamine,[16] poly(vinyl alcohol),[17] and aramid fiber,[14] due to the formation of hydrogen bonds between the OH and F groups on the $Ti_3C_2T_x$ MXene surface and NH_2, OH, and COOH groups of the polymers. The gelatin/MXene multifunctional sensing platform could work for 7 days at room temperature.[18] The development of a gelatin/MXene multifunctional sensing platform for working over 30 days has been rarely reported.

Of these sensors, actuation, due to structural deformation and physical motion, represents a unique sensing mechanism in intelligent control, visualization, and wireless sensing.[19−21] Controllable and rapid actuation can be achieved by exploiting the different thermal expansion of heterogeneous layers.[22−24]

Received: August 7, 2022
Revised: March 19, 2023
Published: April 6, 2023

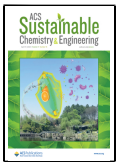

https://doi.org/10.1021/acssuschemeng.2c04712
ACS Sustainable Chem. Eng. 2023, 11, 5834−5844

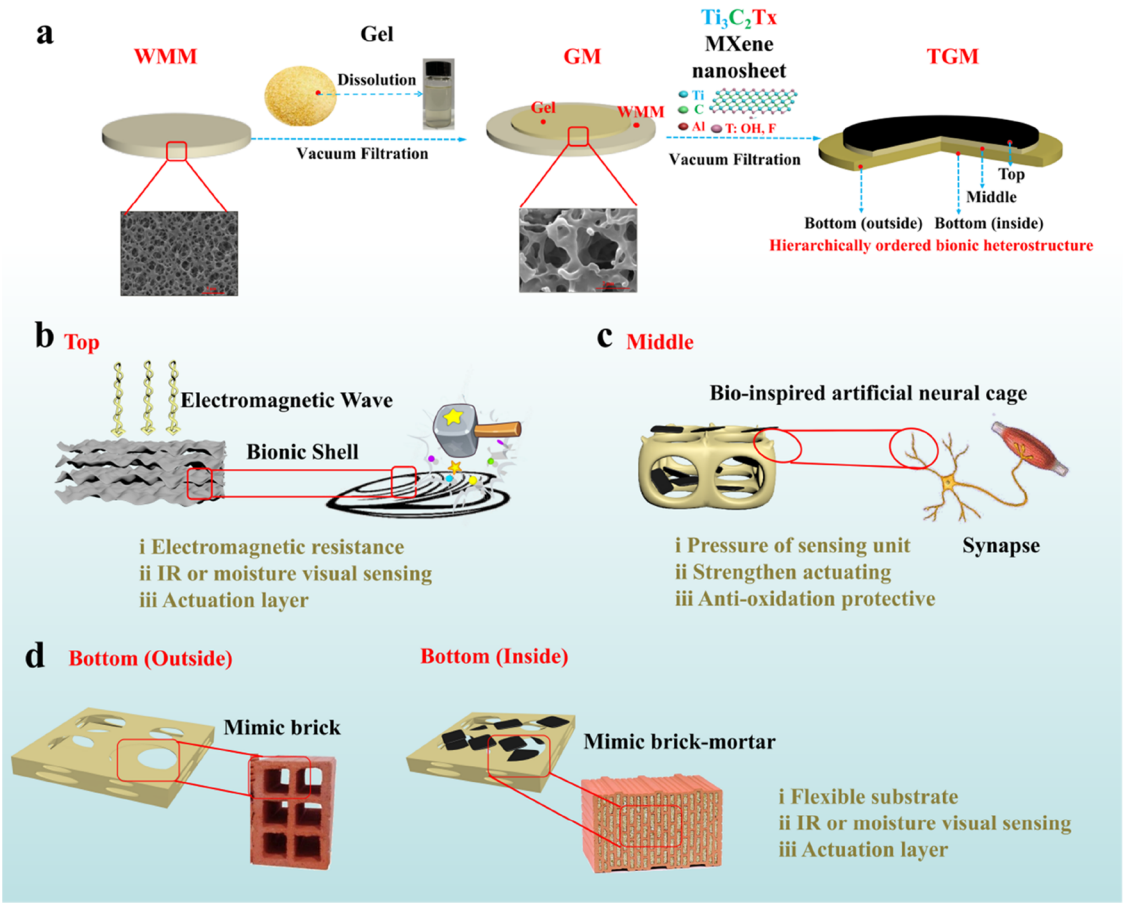

Figure 1. Fabrication process and material structure of the TGM composite. (a) Schematic illustration of the fabrication procedure. (b) The top layer of the TGM bionic shell. (c) The middle layer of the TGM showing the bioinspired artificial neural cages. (d) The bottom layer of the TGM showing (outside) brick and (inside) brick-mortar mimics.

For example, a heterogeneous structure composed of $Ti_3C_2T_x$ MXene@paper and polyethylene has been found to actuate under near-infrared (NIR) light irradiation (350 mW/cm^2) or upon exposure to moisture[25] because the remarkable photothermal and hygroscopic properties of $Ti_3C_2T_x$ MXene lead to effective structural expansion.

Furthermore, as electromagnetic interference (EMI) has become an environmental issue, it is critical to endow flexible sensors with anti-interference performance,[26,27] in comparison to traditional metal-based EMI shielding materials.[28,29] Composite materials based on $Ti_3C_2T_x$ MXene are known to exhibit high EMI shielding effectiveness (EMI SE). However, the high reflection of EMI by MXene will produce secondary electromagnetic pollution, and structural engineering of the materials is needed so as to enhance electromagnetic absorption.[30,31]

Despite substantial progress in recent years, it remains a great challenge to prepare an all-in-one eco-friendly flexible sensor that intrinsically integrates these features of outstanding sensing, tunable optical actuating, and excellent EMI SE. The bionic structure introduced into sensor would be enhanced the intrinsic functions or gave the new functions of the sensor. Herein, we report the design and fabrication of a flexible advanced sensor based on a hierarchically ordered bionic heterostructure by the layer-by-layer assembly of $Ti_3C_2T_x$ MXene, gelatin, and water-based multiporous membrane (WMM), which was $Ti_3C_2T_x$ MXene−gelatin−WMM (referred to as TGM). The top layer is a multilayer structure with a bionic impact resistance of a "shell" for improving EMI shielding, the middle layer is an artificial neural cage and synapsis structure with bioinspired information transmission of "synapses" for sensing sensitivity, and the bottom layer is a multiporous structure which mimics light weight and high strength of a "brick" for stable sensing. The resulting TGM trilayer composite can be used for the detection of multiple stimuli and service environments based on electrical conductivity and actuation, and exhibit excellent EMI shielding, great degradation, and minimal impacts on plant growth. Practical applications are also demonstrated by using the composite sensor as a flexible wearable and smart switch for real-time monitoring of human motions, environmental humidity, and temperature.

RESULTS AND DISCUSSION

Preparation of Bionic Heterostructures and Structural Characterization. The fabrication process of the TGM composite is illustrated in Figure 1a, where the hierarchically ordered bionic heterostructure was prepared via a layer-by-layer assembly of $Ti_3C_2T_x$ MXene, gelatin, and WMM. First, WMM with a multiporous morphology was selected as the flexible substrate due to its mechanical flexibility, chemical durability, biocompatibility, and biodegradability. The WMM (pore size 0.45 μm) is a mixed fiber resin membrane mainly composed of nitrocellulose and cellulose acetate. A gelatin solution was deposited onto WMM by vacuum filtration to

https://doi.org/10.1021/acssuschemeng.2c04712
ACS Sustainable Chem. Eng. 2023, 11, 5834−5844

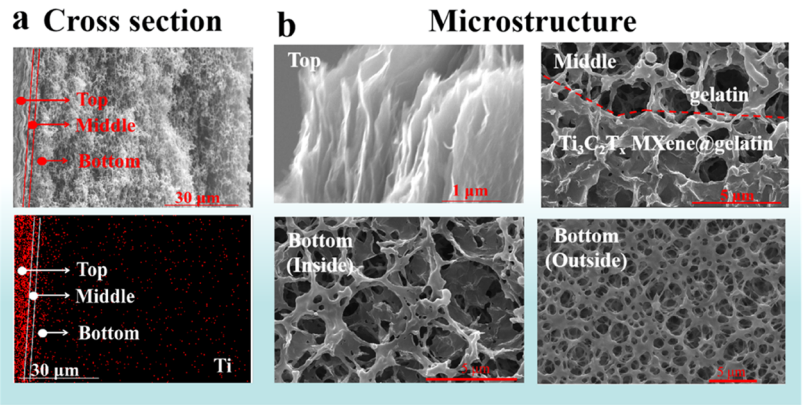

Figure 2. Structure characterization of the TGM. (a) (top) Cross-section of the hierarchical bionic structure and (bottom) Ti elemental map. (b) Microstructure from the top to the bottom.

construct an artificial neural cage structure. The bilayer film (gelatin/WMM, referred to as GM) was composed of a top layer of gelatin and a bottom layer of WMM. The thickness, mean pore diameter, and morphology of the resulting GM can be readily manipulated by varying the loading of gelatin, as manifested in scanning electron microscopy (SEM) measurements of the sample surface and cross-section. From Figure S1, it can be seen that with an increased loading of gelatin, the thickness of GM increased accordingly.

In addition, $Ti_3C_2T_x$ MXene nanosheets were selected as the substrate due to the high electrical conductivity and were deposited onto the GM bilayer also by vacuum filtration, producing a trilayer structure (TGM). The $Ti_3C_2T_x$ MXene nanosheets were obtained by selectively etching Al from the multilayer structure of Ti_3AlC_2 in a solution of LiF and HCl (Figure S2a,b, inset of Figure S2c). In comparison with Ti_3AlC_2 MAX, the X-ray diffraction (XRD) patterns of the $Ti_3C_2T_x$ MXene nanosheets exhibited a clear shift of the (002) peak from 2θ = 9.6 to 6.0°, and concurrently, the peak for the Al layer at 2θ = 39° disappeared (Figure S2c). Transmission electron microscopy (TEM) measurements clearly showed an ultrathin structure of the resulting $Ti_3C_2T_x$ MXene nanosheets with a lateral size of ca. 5 μm and uniform distribution of Ti, as evidenced in elemental mapping analysis (Figure S2d). Consistent results were obtained in selected area electron diffraction (SAED) measurements (inset of Figure S2b$_3$), which indicates that the $Ti_3C_2T_x$ MXene nanosheets retained the hexagonal basal plane symmetry of Ti_3AlC_2 MAX.

The structure of the TGM composite was first characterized by SEM measurements (Figure 2), where a hierarchical bionic heterostructure can be clearly seen. From the cross-sectional SEM image and Ti elemental map in Figure 2a, the $Ti_3C_2T_x$ MXene nanosheets can be seen to mostly reside in the top layer of TGM, with a moderate amount in the middle layer and only a minimal content in the bottom layer. In the hierarchical structure (Figure 2b), the top layer was a multilayer bionic "shell" of $Ti_3C_2T_x$ MXene (Figures 1b and 2b—top), the middle layer was $Ti_3C_2T_x$ MXene@gelatin with flexible cages and synapses (Figures 1c and 2b—middle), the inside of the bottom layer was $Ti_3C_2T_x$ MXene@WMM with an ordered multipore structure coated with $Ti_3C_2T_x$ MXene "brick-mortar" mimic (Figures 1d and 2b—bottom inside), and the outside of the bottom layer was WMM with an ordered multipore "brick"-mimic structure (Figures 1d and 2b—bottom outside). This unique hierarchical heterostructure endows the composite film with excellent sensing performances toward multiple stimulations, as detailed below.

From the XRD patterns in Figure S3, $Ti_3C_2T_x$ MXene can be seen to exhibit a well-defined peak at 2θ = 6°, suggesting a relatively crystalline structure. For the bilayer GM, two broad diffraction peaks emerged at 2θ = 9 and 21° arising from the amorphous gelatin and the triple-helix structure,[29] respectively. All of these diffraction peaks can be resolved in TGM, but the peak intensities were substantially weakened, suggesting an increasingly amorphous structure within the trilayer composite.

Pressure Sensing. The pressure sensing performance of the TGM composite was then tested under different conditions at the same input voltage of 1.0 V. Figure 3a shows the schematic of the TGM-based pressure sensing device in air by detecting the relative change of the electrical resistance, $\Delta R/R_0$, with $\Delta R = R - R_0$, where R_0 and R stand for the resistance in the absence and presence of applied pressure, respectively. The sensitivity is evaluated by using the indicator gauge factor (GF), GF = $(\Delta R/R_0)/\Delta P$, where ΔP refers to the change of pressure (Figure S4). Figure 3b shows the sensing responses at different applied pressures. It can be seen that $\Delta R/R_0$ varied from 0.15 to 3.6 with the pressure varied from 3.6 to 18.0 kPa, and GF reached 17.8 kPa^{-1} at 3.6−7.8 kPa and 5.6 kPa^{-1} at 7.8−18.0 kPa (Figure 3c). Notably, the TGM could respond readily to pressure (3.6−18.0 kPa) in both discontinuous (Figure S5a) and reciprocating (Figure S5b) modes. The results demonstrated that the TGM could clearly and quickly reflect the variation of the working modes under different pressures in time, with a wide detection range, high accuracy, and good resolution. The TGM also maintained a rapid real-time response at varied frequencies (1−5 Hz) (Figure 3d). At the applied pressure of 40.0 kPa, the TGM sensor shows a short response time of 178 ms and a recovery time of 155 ms (Figure S6). The stability test was then tested by repeating 2000 cycles at a pressure of 7.2 kPa (Figure 3e). Significantly, the TGM retained an excellent sensing performance for up to 30 d (Figure S7), likely because of sufficient protection of $Ti_3C_3T_x$ MXene against oxidation (Figure S8).

The pressure sensing performance was also tested under water (Figure 3f). The electrical current was measured in response to the underwater pressure (25 °C, pH 7.0), and the sensing property was characterized by measuring the relative current change $(\Delta I/I_0)$, with $\Delta I = I - I_0$, where I_0 and I stand for the current before and after the application of pressure, respectively, and GF = $(\Delta I/I_0)/\Delta P$ (Figure S9). From Video S1, the TGM can be seen to show a good relationship between

https://doi.org/10.1021/acssuschemeng.2c04712
ACS Sustainable Chem. Eng. 2023, 11, 5834−5844

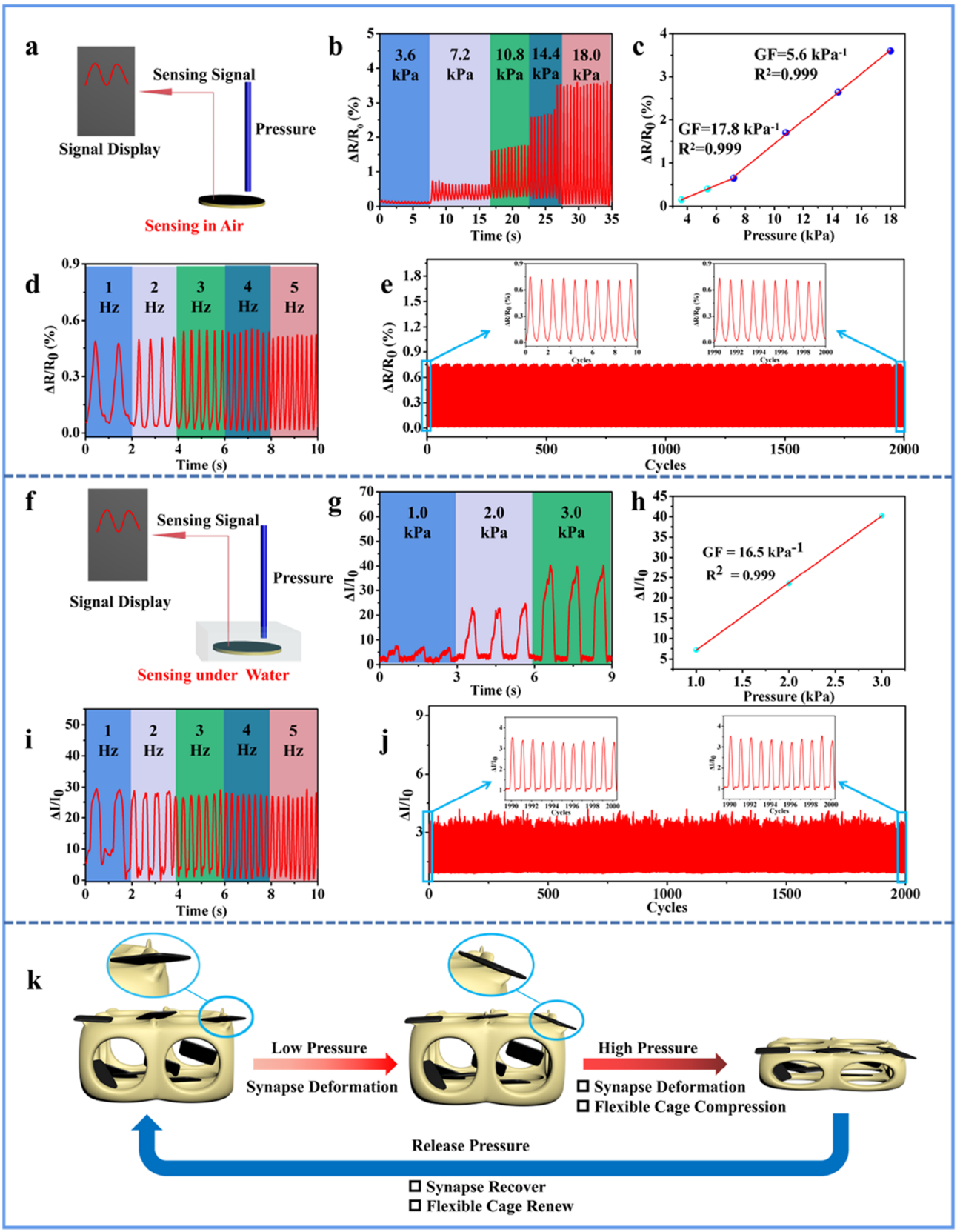

Figure 3. Testing device schematic of pressure sensing using the TGM sensor (a) in air, (b) at different pressures, (c) GF at different pressures, (d) at different frequencies, and (e) stability test of the sensing property when conducting repeated to 2000 cycles at a pressure of 7.2 kPa. (f) Schematic of underwater pressure sensing, (g) at different pressures, (h) GF at 1.0−3.0 kPa, (i) at different frequencies, (j) stability test of the sensing property when conducting repeated 2000 cycles at a pressure of 1.0 kPa. (k) Schematic diagram of the pressure sensing mechanism.

https://doi.org/10.1021/acssuschemeng.2c04712
ACS Sustainable Chem. Eng. 2023, 11, 5834−5844

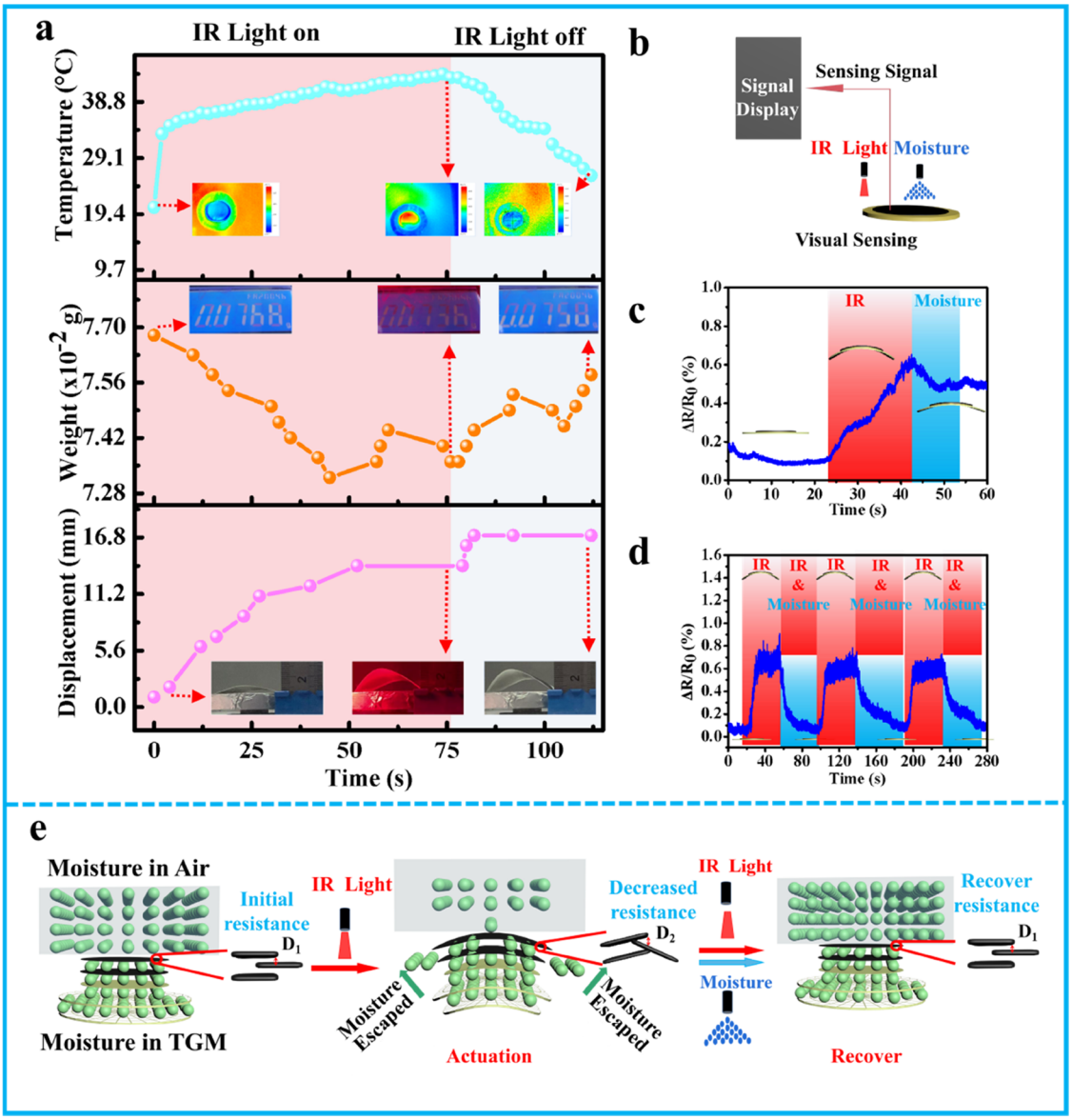

Figure 4. Actuation performance of TGM. (a) Variations of temperature, weight, and displacement of TGM under IR light stimulation. Insets are the corresponding (top) thermal images, (middle) weight photographs, and (bottom) bending motion pictures. (b) Testing device schematic under IR or moisture stimulations. (c) $\Delta R/R_0$ of TGM under IR or moisture stimulations. (d) Sensing tests in three repeated cycles of IR and IR + moisture stimulations. (e) Schematic diagram of actuation and IR or moisture sensing.

the real-time current and underwater pressure. Figure S10 compares the $\Delta I/I_0$ in water and in air. It can be seen that $\Delta I/I_0$ in air (1.0042) was somewhat smaller than that at 10 cm underwater (1.0047), and $\Delta I/I_0$ decreased with increasing underwater depth (up to 50 cm, Figure S11). Figure 3g shows the sensing response to different pressures at 50 cm underwater, where the $\Delta I/I_0$ varied from 7.2 to 40.3 and GF reached up to 16.5 kPa^{-1} with the pressure varied from 1.0 to 3.0 kPa (Figure 3h). The TGM retained a rapid real-time response within the frequency range of 1−5 Hz (Figure 3i) and featured a short response time of 156 ms and recovery time of 174 ms under 40.0 kPa (Figure S12). The TGM also demonstrated good stability in 2000 cycles at the pressure of 7.2 kPa (Figure 3j).

In the above pressure sensing (Figure 3k), the middle layer of $Ti_3C_2T_x$ MXene@gelatin most likely played a major role as it contained arrays of artificial neural cages with synapses (Figures 1 and 2). At low pressures (3.6−7.2 kPa in air and 1.0−3.0 kPa under water), the synapse structure of gelatin is tilted and squashed, leading to a change of the shape of the $Ti_3C_2T_x$ MXene nanosheets in the top and middle layers, and hence the conductive path and resistance of the TGM composite. At higher pressures (7.2−18.0 kPa in air), the flexible cages were compressed, rendering the inside $Ti_3C_2T_x$ MXene of $Ti_3C_2T_x$ MXene@gelatin to be in contact with each other, and hence a change of the electrical conductivity. When the applied pressure was removed, the synapse and flexible cage returned to the original shape, recovering the conduction path and resistance of $Ti_3C_2T_x$ MXene.

To further demonstrate the applications of TGM as a flexible wearable sensor, it was cut into small pieces in the size of 80 mm × 80 mm × 0.2 mm, which were then attached to the clothing of an adult tester weighing 60.0 kg to detect the sensing properties in different activities. The TGM sensor was

https://doi.org/10.1021/acssuschemeng.2c04712
ACS Sustainable Chem. Eng. 2023, 11, 5834−5844

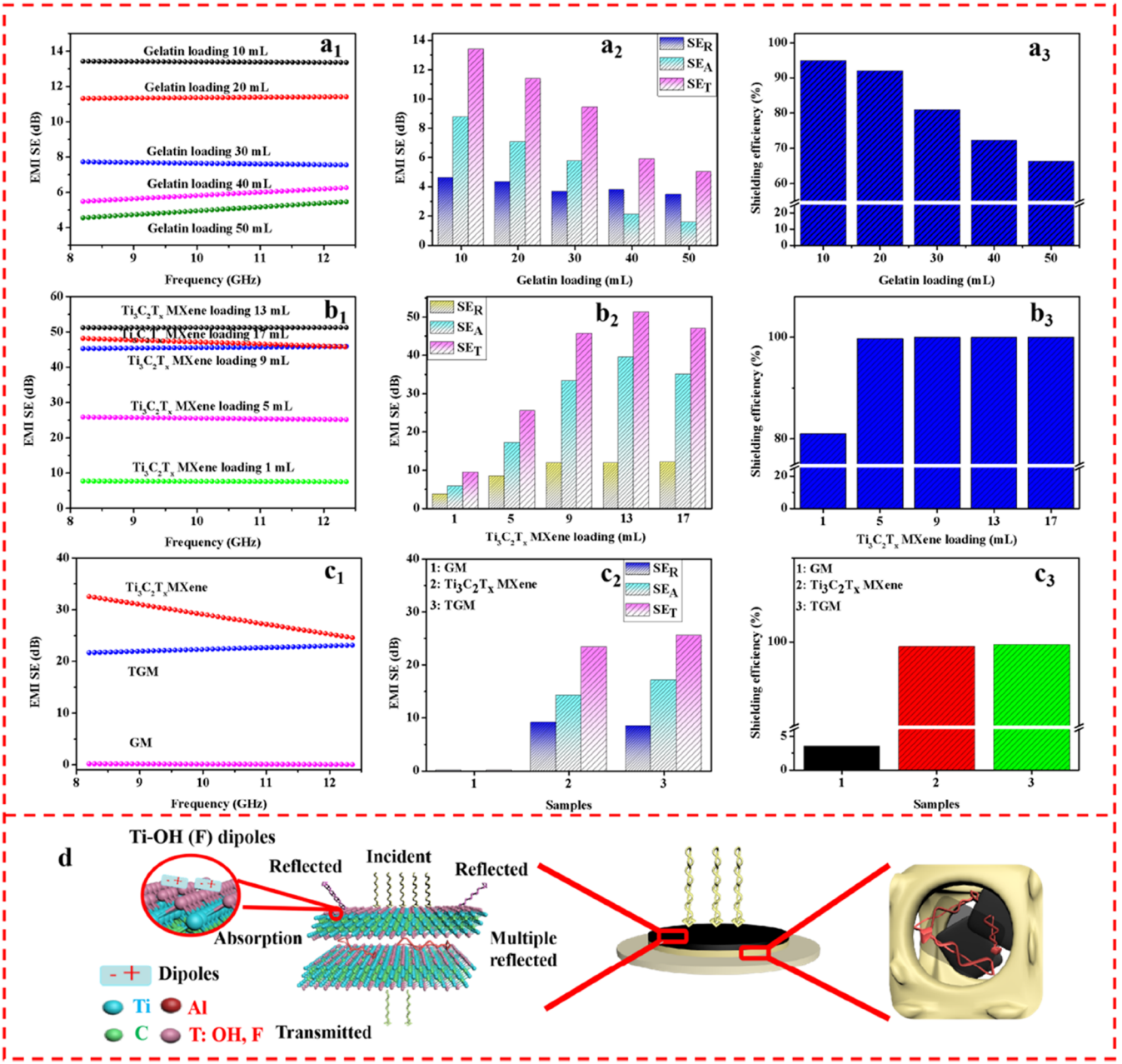

Figure 5. Electromagnetic interference shielding of TGM at different loadings of (a) gelatin and (b) $Ti_3C_2T_x$ MXene in the TGM films. (c) Shielding performance of $Ti_3C_2T_x$ MXene, GM, and TGM. Panels (1) are EMI shielding, panels (2) are total EMI SE (SE_T), microwave reflection (SE_R), and microwave absorption (SE_A), and panels (3) are shielding efficiencies. (d) The EMI SE mechanism of TGM.

used to monitor and record the body motions, including neck, elbow, wrist, finger, knee, and ankle (Figure S13). Notably, the shape of the TGM sensor remained unchanged after the activities. The neck sensing results showed rapid and unique responses to different bending angles (i.e., 105, 130, and 145°). Similar results were obtained for the elbow, when it was bent by 30, 90, and 120°. The TGM also exhibited outstanding electrical signals for fingers, wrists, etc. Note that the TGM could be attached to a sock to monitor the walk, run, and jump of the human tester, displaying stable and distinctly different electrical signals for different sports (Figure S14). Taken together, the results show that TGM could be used as a flexible wearable sensor, retaining a stable relative resistance and hence outstanding sensing performance in monitoring human motions.

Actuation Performance. As shown in Video S2 and Figure 4a, the TGM can also actuate under IR stimulation, where the change of temperature and weight, and physical displacement can be measured by a thermal imager, electronic balance, and ruler. Upon IR irradiation (48 mW/cm^2) for 76 s, the TGM showed an increase of the temperature from 20.6 to 43.3 °C, its weight decreased from 0.0768 to 0.0754 g, and the actuation displacement rose from 0 to 16 mm. The mass loss is likely due to the temperature increase that led to loss of the moisture from the concentric circle structure (Figures 1 and 2).

We then studied the effects of IR, moisture, and IR plus moisture on the actuation performance. From Video S3 and Figure S15a, the actuation rate of thermal expansion under IR irradiation was estimated to be 0.2 mm/s before (step I) and

https://doi.org/10.1021/acssuschemeng.2c04712
ACS Sustainable Chem. Eng. 2023, 11, 5834−5844

0.8 mm/s after exposure to moisture (step III), and the actuation rate of hygroscopic expansion under moisture was 0.46 mm/s from the $Ti_3C_2T_x$ MXene side of the TGM.[32] The actuation rate was clearly different under the same IR irradiation but at different humidities, probably because the refilling (evaporation) of moisture led to hygroscopic expansion (shrinkage).

The actuation behaviors were also tested under heated moistures. The actuating rates of TGM were estimated to be 0.5 mm/s with ambient moisture (step II, Figure S15a) and increased drastically to 1.0 mm/s with both IR and moisture (step II, Figure S15b) from the $Ti_3C_2T_x$ MXene side, suggesting a significant effect of moisture temperature on the actuation rate. Additionally, the actuating and recovery rates of the TGM were faster when TGM was treated with heated moisture from the WMM side (16.3 and 8.2 mm/s) than from the $Ti_3C_2T_x$ MXene side (3.0 and 4.3 mm/s) (Figure S15c and Video S4). This may be ascribed to the enhanced porosity and hygroscopicity of WMM that facilitates moisture exchange, in comparison with $Ti_3C_2T_x$ MXene (Figure 1).

Notably, the tunable actuation and excellent sensing of TGM can be readily integrated to dynamically monitor the ambient temperature and humidity in a visual manner. The device schematic is shown in Figure 4b for the IR and moisture visual sensing by concurrently recording the change of $\Delta R/R_0$ and shape. It can be seen from Figure 4c that the $\Delta R/R_0$ and shape remained unchanged without IR or moisture (from 0 to 20 s); yet when the IR light was turned on (from 20 to 42 s), the TGM became bending up, along with a nonzero $\Delta R/R_0$. When the IR light was turned off and moisture remained on (from 42 to 46 s), the TGM began to recover in shape, and the $\Delta R/R_0$ also decreased. When moisture was on from 46 to 54 s, the $\Delta R/R_0$ and shape of the TGM would hold on even if the moisture was turned off. The $\Delta R/R_0$ change coincided with that in the actuation of the sensor under both IR and moisture stimuli. The visual sensing was repeated in three IR − IR + moisture cycles, and the signals remained highly stable and reproducible (Figure 4d).

The mechanism of actuation and visual sensing is shown in Figure 4e. The actuation is likely due to hygroscopic expansion, where the moisture was exchanged between the TGM and the ambient. Under IR irradiation, the moisture was evaporated from the TGM, and the mass loss led to shrinkage and actuation. With both IR and moisture, the TGM was filled with the moisture in air, which recovered the shape due to hygroscopic expansion. Such different actuation rates under the IR and moisture stimulations also led to a change of the electrical resistance. When the TGM was actuated under IR, the layer distance of $Ti_3C_2T_x$ MXene nanosheets increased, lengthening the conductive paths and increasing the resistance, which led to an increased $\Delta R/R_0$. When the TGM was recovered under the IR + moisture stimulations, the response was reversed. Such structural evolutions were confirmed in XRD measurements (Figure S16).

Motivated by the above results, one can envision that TGM can serve as a smart switch to monitor the air temperature and moisture in various weather conditions, such as high tides, storms, typhoons, etc. In fact, this was demonstrated with an assembly consisting of a TGM composite film and a light-emitting diode (LED) light for the monitoring of fog and air temperature in smart self-driving (Video S5). Likewise, ambient humidity can be monitored as a smart switch (Video S6).

Electromagnetic Shielding. The TGM also exhibited a remarkable EMI SE within the frequency range of 8.2−12.4 GHz (X-band). Figure 5a shows the EMI SE of the TGM films prepared at different loadings of gelatin (Figure S1). With the increasing content of gelatin, the EMI shielding (Figure 5a_1) and EMI SE (Figure 5a_3) decreased, respectively, from 13.5 to 5 dB and 95.12 to 66.59% with the loading of gelatin increased from 10 to 50 mL (concentration 0.4 mg/mL). To clarify the role of gelatin in the EMI SE mechanism, the total EMI shielding effectiveness (SE_T), microwave absorption (SE_A), and microwave reflection (SE_R) are calculated using eqs S1−S6 and are depicted in Figure 5a_2. It can be seen that with an increasing gelatin content, SE_T and SE_A exhibited a significant decrease, but SE_R remained essentially unchanged. This coincided with the formation of denser artificial neural cages in the gelatin with a reduced pore size (Figures 1 and S1), which was conducive to the penetration of $Ti_3C_2T_x$ MXene into the gelatin cages, and hence decreased the surface electrical conductivity (Figure S17) and the eventual EMI SE (eq S7).

Figure 5b shows the EMI SE of the TGM films prepared at different loadings of $Ti_3C_2T_x$ MXene (Figure S18). The EMI shielding (Figure 5b_1) initially increased from 7.6 dB at the loading of 1 mL of $Ti_3C_2T_x$ MXene to 52.0 dB at 13 mL (concentration 0.5 mg/mL) but then decreased to 47.7 dB at 17 mL, and concurrently, the EMI SE (Figure 5b_3) was ca. 80% at 1 mL and then remained essentially unchanged at 99.99% at higher loadings of $Ti_3C_2T_x$ MXene. The SE_T and SE_A showed the same trend reaching a maximal EMI SE at 13 mL, whereas SE_R remained mostly constant at loadings over 9 mL (Figure 5b_2). Because of the highly conductive $Ti_3C_2T_x$ MXene, when the electromagnetic wave reached the top layer of the TGM film, the incident wave was reflected off to the air due to the discontinuity of impedance at the air/$Ti_3C_2T_x$ MXene interface. There are two contributions to the EMI SE of $Ti_3C_2T_x$ MXene. The first is that the highly conductive $Ti_3C_2T_x$ MXene absorbs microwave, and the more $Ti_3C_2T_x$ MXene nanosheets were loaded into TGM, the more conductive pathways were formed, and the EMI SE_R became stronger. The other is that the surface of $Ti_3C_2T_x$ MXene contained a number of functional groups (e.g., OH, F, and O) and local defects, which could induce an asymmetric distribution of charge density and generate local dipoles, resulting in the polarization relaxation and enhanced overall shielding effectiveness.

From Figure 5c, one can see that the EMI SE of the bilayer GM films was essentially zero, whereas the EMI shielding and EMI SE of TGM are 25 dB and 99.68%, respectively, suggesting the dominant contribution of $Ti_3C_2T_x$ MXene to EMI shielding. Figure 5d illustrates the EMI SE mechanism of the TGM, which entailed three contributions, high electrical conductivity and surface groups of $Ti_3C_2T_x$ MXene,[33,34] and artificial neural cages of gelatin that attenuated the microwaves by internal multiple reflection and absorption, while the randomly distributed $Ti_3C_2T_x$ MXene might also contribute to the multiple reflection.[35,36] Notably, the TGM exhibited low microwave reflection and high microwave absorption due to the hierarchically ordered structure, which mitigated the problem of secondary pollution during the reflection of electromagnetic waves.

Environmental Impact. The alkaline solution immersion method is also often used to test the degradability of the sensor.[37−39] To evaluate the degradable performance of the

https://doi.org/10.1021/acssuschemeng.2c04712
ACS Sustainable Chem. Eng. 2023, 11, 5834−5844

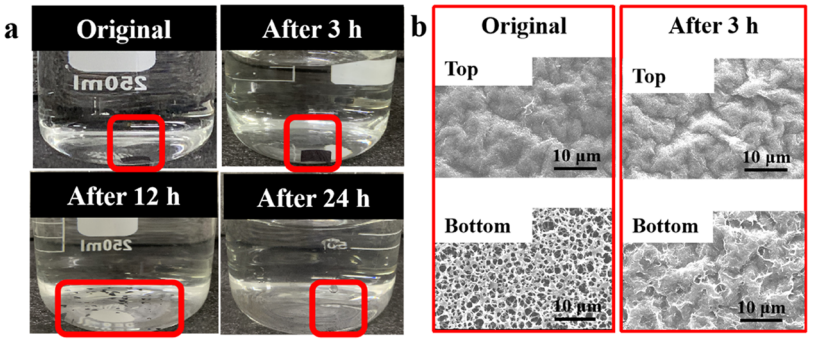

Figure 6. (a) Photographs of the TGM sensor placed in a 0.5 M NaOH solution for different times. (b) The SEM images of the TGM sensor before and after 3 h of degradation.

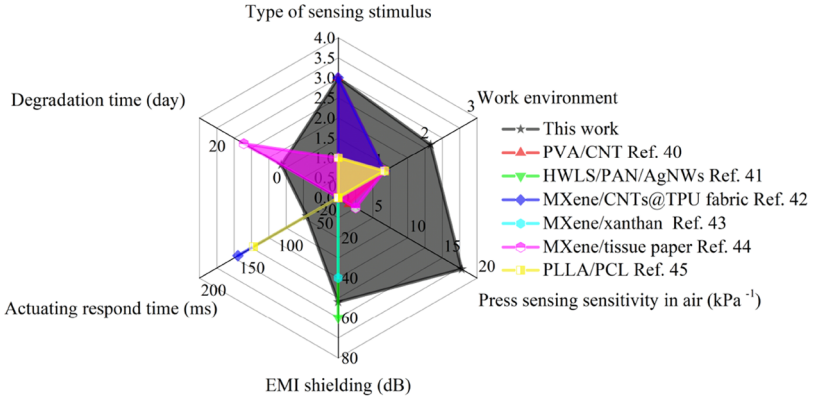

Figure 7. Comparison between this paper and other papers on multifunctional flexible sensors.

TGM sensor, the sensor device was placed into 0.5 M NaOH solution at 25 °C, and the resulting appearance changes were measured. Figure 6a shows photographs of the TGM sensor placed in 0.5 M NaOH solution for different times. As seen from Figure 6a, after 3 h of degradation of TGM, the white part of TGM was WMM, which disappeared, and the NaOH solution became yellow from transparent. After 12 h of degradation, the TGM degraded into small pieces. After 24 h of degradation, TGM basically degraded completely and disappeared. Figure 6b shows the SEM of the TGM sensor placed in 0.5 M NaOH solution before and after 3 h. As seen from Figure 6b, before the 3 h of degradation, the bottom of TGM was a multiporous structure, and the top of TGM was a wrinkled structure. After 3 h of degradation, the multiporous structure bottom of TGM disappeared, and a crack appeared at the top wrinkled structure of TGM. The results show that TGM can be completely degraded by soaking in 0.5 M NaOH solution for 24 h, and the WMM of TGM degrades faster than $Ti_3C_2T_x$ MXene of TGM. The reason why the WMM of TGM degrades faster than the $Ti_3C_2T_x$ MXene is that WMM exhibits porous hydrophilicity, which is conducive to the entry of alkaline water. Then, the alkaline water interrupts the noncovalent bond between cellulose acetate and gelatin, so that the WMM of TGM degrades rapidly. The $Ti_3C_2T_x$ MXene of TGM has dense surface topography, and the −F on the $Ti_3C_2T_x$ MXene surface has a certain hydrophobicity. The alkaline water penetrated into the top layer with difficulty, so the top degraded slowly. These results fully demonstrate that our sensor could be degradable and will not cause any severe harm to the environment. Compared with the literature,[37,39] our sensor only needed 24 h to degrade. This shows that the TGM sensor exhibits good environmental friendliness. Figures S19 and S20 show the TGM sensor without affecting the growth of plant seeds.

As seen from Figure 7, an eco-friendly multifunctional flexible sensor with outstanding properties, including multi-sensing stimulus, more work environment, high EMI shielding, fast actuating response time, and degradation time, was obtained through an integrated functional design. Moreover, the versatility offers distinct advantages over many materials reported in the literature.[40−45]

CONCLUSIONS

In summary, an eco-friendly composite film was prepared by the layer-by-layer assembly of WMM, $Ti_3C_2T_x$ MXene, and gelatin, and exhibited multifunctional sensing, actuation, and EMI shielding. This was ascribed to the formation of a hierarchically ordered bionic heterostructure. The resulting TGM composites demonstrated a stable and sensitive sensing of pressure both in air and under water due to a sensitive variation of the electrical conductivity and could be exploited for the visual monitoring of human physical motions and activities. The TGM composites also exhibited apparent actuation under heat and moisture stimulations and thus could be used as a smart switch in the visual sensing of the change of environmental temperature and humidity. In addition, TGM showed excellent EMI SE and eco-friendliness. These suggest the significant potential of MXene−gelatin composites as a unique all-in-one platform for multifunctional applications.

https://doi.org/10.1021/acssuschemeng.2c04712
ACS Sustainable Chem. Eng. 2023, 11, 5834−5844

MATERIALS AND METHODS

Chemicals and Materials. Titanium aluminum carbide (MAX Ti_3AlC_2 purity of 98%), lithium fluoride (LiF, 99%), and gelatin were purchased from Shanghai Macklin Biochemical Co., Ltd. (Shanghai, China). Hydrofluoric acid (HCl, 36%) was provided by Sinopharm Chemical Reagents Company (China). WMM (pore size 0.45 μm) was obtained from Yamai Glass Instrument Technology Co., LTD. without any further treatment. WMM is a mixed fiber resin membrane mainly composed of nitrocellulose and cellulose acetate.

Preparation of $Ti_3C_2T_x$ MXene Nanosheets. $Ti_3C_2T_x$ MXene was prepared by HCl/LiF etching of Ti_3AlC_2 MAX. Experimentally, 30 mL of concentrated HCl and 1 g of LiF were added into a Teflon cup under magnetic stirring at 5 °C for 20 min. The temperature was then raised to 60 °C, and 1 g of Ti_3AlC_2 MAX was added to the solution for chemical etching. After 24 h, the solution was rinsed with 1 M HCl five times and then with distilled water until the pH was close to 7.0, before centrifugation at 3500 RPM for 20 min, affording $Ti_3C_2T_x$ MXene multilayers. To prepare $Ti_3C_2T_x$ MXene nanosheets, the $Ti_3C_2T_x$ MXene multilayer suspension was sonicated at 10 °C for 60 min, followed by centrifugation at 3500 rpm to separate the $Ti_3C_2T_x$ MXene nanosheets, which were collected and stored in a refrigerator.

Preparation of TGM. A gelatin solution (0.4 g/mL) was prepared and maintained at 40 °C, and a calculated amount (i.e., 10, 20, 30, 40, or 50 mL) was deposited onto the WMM by vacuum filtration. The obtained GM bilayer films were dried naturally. Subsequently, a different amount (i.e., 1, 5, 9, 13, or 17 mL) of $Ti_3C_2T_x$ MXene nanosheets obtained above (0.5 mg/mL) was deposited onto GM also by vacuum filtration, producing a TGM trilayer structure that was used as the active material for the flexible sensor.

Characterization. SEM measurements were conducted using an FEI Quanta 450 scanning electron microscope (SEM, America) with an acceleration voltage of 5 kV. TEM images were obtained with a Tecnai G2 F20 S-Twin transmission electron microscope (TEM) at an acceleration voltage of 200 kV. Infrared spectra were collected with a Bruker Vertex 70 Fourier transformed infrared instrument (FT-IR, German). XRD patterns were acquired using a Bruker D8 Advance diffractometer (Germany) with a working current of 40 mA and voltage of 40 kV, within the 2θ range of 5−60° at a scanning speed of 6° per min. An ST2253 digital four-probe tester (Suzhou Lattice Electronics Co., LTD, China) was used to study the conductivity of all samples. The output power of the IR lamp is 48 mW/cm^2. An infrared imaging study was carried out with a thermal analyzer (Testo 869, Germany). The sensing performance was tested with an electrochemical workstation in connection with a miniature electronic dynamometer, and conductive tape was connected to both sides of the TGM. The SE (dB) of the TGM was investigated using a waveguide specimen holder (length × width × height = 22.86 mm × 10.16 mm × 3.00 mm) using a vector network analyzer (N5230A, Agilent) in the frequency range of 8.2−12.4 GHz. The environmental impact was tested by the methods in which 0.16 g of samples were cut into pieces and planted with wheat in 100 g of soil and lilies in 250 mL of deionized water.

ASSOCIATED CONTENT

Supporting Information

The Supporting Information is available free of charge at https://pubs.acs.org/doi/10.1021/acssuschemeng.2c04712.

Characterization of GM films and $Ti_3C_2T_x$ MXene; XRD patterns of $Ti_3C_2T_x$ MXene; GM and TGM; TGM sensing performance in air or under water; the TGM sensor performance after 7, 15, and 30 d in air; Ti 2p XPS spectra of the TGM sensor (a) before and (b) after 30 days; application of TGM in monitoring and recording of human motions; actuation of TGM; XRD patterns of $Ti_3C_2T_x$ MXene before and after actuation; electrical resistivity of the TGM at different gelatin and $Ti_3C_2T_x$ MXene loadings; wheat grown in soil or lily grown under water in the presence of TGM; and $Ti_3C_2T_x$ MXene, GM, and control (PDF)

Underwater pressure sensing (MP4)

Actuation of TGM by IR irradiation (MP4)

Actuation of TGM by IR irradiation or IR and moisture (MP4)

Actuation of TGM by heated moisture (MP4)

Application of TGM in smart switch (MP4)

Application of TGM in smart driving (MP4)

AUTHOR INFORMATION

Corresponding Authors

Dangge Gao − *College of Bioresources Chemical and Materials Engineering, Shaanxi University of Science &Technology, Xi'an, Shaanxi 710021, China; National Demonstration Center for Experimental Light Chemistry Engineering Education, Shaanxi University of Science &Technology, Xi'an, Shaanxi 710021, China; Xi'an Key Laboratory of Green Chemicals and Functional Materials, Xi'an, Shaanxi 710021, China;* orcid.org/0000-0002-9100-4917; Email: dangge2000@126.com

Jianzhong Ma − *College of Bioresources Chemical and Materials Engineering, Shaanxi University of Science &Technology, Xi'an, Shaanxi 710021, China; National Demonstration Center for Experimental Light Chemistry Engineering Education, Shaanxi University of Science &Technology, Xi'an, Shaanxi 710021, China; Xi'an Key Laboratory of Green Chemicals and Functional Materials, Xi'an, Shaanxi 710021, China;* orcid.org/0000-0003-0512-702X; Email: majz@sust.edu.cn

Shaowei Chen − *Department of Chemistry and Biochemistry, University of California, Santa Cruz, California 96064, United States;* orcid.org/0000-0002-3668-8551; Email: shaowei@ucsc.edu

Authors

Chi Zheng − *College of Bioresources Chemical and Materials Engineering, Shaanxi University of Science &Technology, Xi'an, Shaanxi 710021, China; National Demonstration Center for Experimental Light Chemistry Engineering Education, Shaanxi University of Science &Technology, Xi'an, Shaanxi 710021, China; Xi'an Key Laboratory of Green Chemicals and Functional Materials, Xi'an, Shaanxi 710021, China*

Bin Lyu − *College of Bioresources Chemical and Materials Engineering, Shaanxi University of Science &Technology, Xi'an, Shaanxi 710021, China; National Demonstration Center for Experimental Light Chemistry Engineering Education, Shaanxi University of Science &Technology, Xi'an, Shaanxi 710021, China; Xi'an Key Laboratory of Green Chemicals and Functional Materials, Xi'an, Shaanxi 710021, China;* orcid.org/0000-0001-8785-2246

Yingying Zhou − *College of Bioresources Chemical and Materials Engineering, Shaanxi University of Science &Technology, Xi'an, Shaanxi 710021, China; National Demonstration Center for Experimental Light Chemistry Engineering Education, Shaanxi University of Science &Technology, Xi'an, Shaanxi 710021, China; Xi'an Key Laboratory of Green Chemicals and Functional Materials, Xi'an, Shaanxi 710021, China*

Ailin Zhang − *College of Bioresources Chemical and Materials Engineering, Shaanxi University of Science &Technology,*

Xi'an, Shaanxi 710021, China; National Demonstration Center for Experimental Light Chemistry Engineering Education, Shaanxi University of Science &Technology, Xi'an, Shaanxi 710021, China; Xi'an Key Laboratory of Green Chemicals and Functional Materials, Xi'an, Shaanxi 710021, China

Yu Gu − *College of Bioresources Chemical and Materials Engineering, Shaanxi University of Science &Technology, Xi'an, Shaanxi 710021, China; National Demonstration Center for Experimental Light Chemistry Engineering Education, Shaanxi University of Science &Technology, Xi'an, Shaanxi 710021, China; Xi'an Key Laboratory of Green Chemicals and Functional Materials, Xi'an, Shaanxi 710021, China*

Davida Briana DuBois − *Department of Chemistry and Biochemistry, University of California, Santa Cruz, California 96064, United States;* orcid.org/0000-0002-2612-3717

Complete contact information is available at: https://pubs.acs.org/10.1021/acssuschemeng.2c04712

Notes

The authors declare no competing financial interest.

■ ACKNOWLEDGMENTS

The work was funded by the National Natural Science Foundation of China (21878182), the Shaanxi Provincial "Special Support Plan for High-level Talents", Innovation Capability Support Program of Shaanxi (Program No. 2021TD-16), Science Foundation for Distinguished Young Scholars of Shaanxi Natural Science Basic Research Program (2020JC-47), and Shaanxi Province key research and development plan (2021GY-200), Key Project of Natural Science Basic Research Program of Shaanxi Province (Special Support) (2023JC-XJ-12).

■ REFERENCES

(1) Sanderson, K. Electronic Skin: From Flexibility to a Sense of Touch. *Nature* **2021**, *591*, 685−687.

(2) Liu, H. D.; Zhang, H. J.; Han, W. Q.; Lin, H. J.; Li, R. Z.; Zhu, J. X.; Huang, W. 3D Printed Flexible Strain Sensors: From Printing to Devices and Signals. *Adv. Mater.* **2021**, *33*, No. 2004782.

(3) Xu, S.; Jayaraman, A.; Rogers, J. A. Skin Sensors Are the Future of Health Care. *Nature* **2019**, *571*, 319−321.

(4) Oh, Y. S.; Kim, J. H.; Xie, Z. Q.; Cho, S.; Han, H.; Jeon, S. W.; Park, M.; Namkoong, M.; Avila, R.; Song, Z.; Lee, S. U.; Ko, K.; Lee, J.; Lee, J. S.; Min, W. G.; Lee, B. J.; Choi, M.; Chung, H. U.; Kim, J.; Han, M. D.; Koo, J.; Choi, Y. S.; Kwak, S. S.; Kim, S. B.; Kim, J.; Choi, J.; Kang, C. M.; Kim, J. U.; Kwon, K.; Won, S. M.; Baek, J. M.; Lee, Y.; Kim, S. Y.; Lu, W.; Vazquez-Guardado, A.; Jeong, H.; Ryu, H. J.; Lee, G.; Kim, K.; Kim, S.; Kim, M. S.; Choi, J.; Choi, D. Y.; Yang, Q. S.; Zhao, H. B.; Bai, W. B.; Jang, H.; Yu, Y. J.; Lim, J.; Guo, X.; Kim, B. H.; Jeon, S.; Davies, C.; Banks, A.; Sung, H. J.; Huang, Y. G.; Park, I.; Rogers, J. A. Battery-free, Wireless Soft Sensors for Continuous Multi-site Measurements of Pressure and Temperature from Patients at Risk for Pressure Injuries (vol 12, 6827, 2021). *Nat. Commun.* **2021**, *12*, No. 5008.

(5) Boutry, C. M.; Beker, L.; Kaizawa, Y.; Vassos, C.; Tran, H.; Hinckley, A. C.; Pfattner, R.; Niu, S. M.; Li, J. H.; Claverie, J.; Wang, Z.; Chang, J.; Fox, P. M.; Bao, Z. N. Biodegradable and Flexible Arterial-pulse Sensor for the Wireless Monitoring of Blood Flow. *Nat. Biomed. Eng.* **2019**, *3*, 47−57.

(6) Liao, H.; Guo, X. L.; Wan, P. B.; Yu, G. H. Conductive MXene Nanocomposite Organohydrogel for Flexible, Healable, Low-Temperature Tolerant Strain Sensors. *Adv. Funct. Mater.* **2019**, *29*, No. 1904507.

(7) Li, E.; Pan, Y. M.; Wang, C. F.; Liu, C. T.; Shen, C. Y.; Pan, C. F.; Liu, X. H. Asymmetric Superhydrophobic Textiles for Electromagnetic Interference Shielding, Photothermal Conversion, and Solar Water Evaporation. *ACS Appl. Mater. Interfaces* **2021**, *13*, 28996−29007.

(8) Yang, X.; Wang, Q.; Zhu, K.; Ye, K.; Wang, G. L.; Cao, D. X.; Yan, J. 3D Porous Oxidation-Resistant MXene/Graphene Architectures Induced by In Situ Zinc Template toward High-Performance Supercapacitors. *Adv. Funct. Mater.* **2021**, *31*, No. 2101087.

(9) Yue, O.; Wang, X. C.; Liu, X. H.; Hou, M. D.; Zheng, M. H.; Wang, Y. Y.; Cui, B. Q. Spider-Web and Ant-Tentacle Doubly Bio-Inspired Multifunctional Self-Powered Electronic Skin with Hierarchical Nanostructure. *Adv. Sci.* **2021**, *8*, No. 2004377.

(10) Sun, Q. Z.; Wang, L.; Yue, X. P.; Zhang, L. R.; Ren, G. Z.; Li, D. H.; Wang, H. C.; Han, Y. J.; Xiao, L. L.; Lu, G.; Yu, H. D.; Huang, W. Fully Sustainable and High-performance Fish Gelatin-based Triboelectric Nanogenerator for Wearable Movement Sensing and Human-machine Interaction. *Nano Energy* **2021**, *89*, No. 106329.

(11) Han, Y. J.; Han, Y. F.; Zhang, X. P.; Li, L.; Zhang, C. W.; Liu, J. H.; Lu, G.; Yu, H. D.; Huang, W. Fish Gelatin Based Triboelectric Nanogenerator for Harvesting Biomechanical Energy and Self-Powered Sensing of Human Physiological Signals. *ACS Appl. Mater. Interfaces* **2020**, *12*, 16442−16450.

(12) Zhang, X. P.; Ye, T. Y.; Meng, X. H.; Tian, Z. H.; Pang, L. H.; Han, Y. J.; Li, H.; Lu, G.; Xiu, F.; Yu, H. D.; Liu, J. Q.; Huang, W. Sustainable and Transparent Fish Gelatin Films for Flexible Electroluminescent Devices. *ACS Nano* **2020**, *14*, 3876−3884.

(13) Charles, A. D. M.; Rider, A. N.; Brown, S. A.; Wang, C. H. Multifunctional Magneto-polymer Matrix Composites for Electromagnetic Interference Suppression, Sensors and Actuators. *Prog. Mater. Sci.* **2021**, *115*, No. 100705.

(14) Wang, L.; Zhang, M. Y.; Yang, B.; Tan, J. J.; Ding, X. Y. Highly Compressible, Thermally Stable, Light-Weight, and Robust Aramid Nanofibers/Ti3AlC2 MXene Composite Aerogel for Sensitive Pressure Sensor. *ACS Nano* **2020**, *14*, 10633−10647.

(15) Qin, M. H.; Yuan, W. F.; Zhang, X. M.; Cheng, Y. Z.; Xu, M. J.; Wei, Y.; Chen, W. Y.; Huang, D. Preparation of PAA/PAM/MXene/TA Hydrogel with Antioxidant, Healable Ability as Strain Sensor. *Colloids Surf., B* **2022**, *214*, No. 112482.

(16) Hatter, C. B.; Shah, J.; Anasori, B.; Gogotsi, Y. Micromechanical Response of Two-dimensional Transition Metal Carbonitride (MXene) Reinforced Epoxy Composites. *Composites, Part B* **2020**, *182*, No. 107603.

(17) Lee, S.; Kim, E. H.; Yu, S.; Kim, H.; Park, C.; Lee, S. W.; Han, H.; Jin, W.; Lee, K.; Lee, C. E.; Jang, J.; Koo, C. M.; Park, C. Polymer-Laminated Ti3C2Tx MXene Electrodes for Transparent and Flexible Field-Driven Electronics. *ACS Nano* **2021**, *15*, 8940−8952.

(18) Wang, X. M.; Wang, X. L.; Yin, J. J.; Li, N.; Zhang, Z. L.; Xu, Y. W.; Zhang, L. X.; Qin, Z. H.; Jiao, T. F. Mechanically Robust, Degradable and Conductive MXene-composited Gelatin Organohydrogel with Environmental Stability and Self-adhesiveness for Multifunctional Sensor. *Composites, Part B* **2022**, *241*, No. 110052.

(19) Zhao, H. T.; Hu, R.; Li, P.; Gao, A. Z.; Sun, X. T.; Zhang, X. H.; Qi, X. J.; Fan, Q.; Liu, Y. D.; Liu, X. Q.; Tian, M. W.; Tao, G. M.; Qu, L. J. Soft Bimorph Actuator with Real-time Multiplex Motion Perception. *Nano Energy* **2020**, *76*, No. 104926.

(20) Manzoor, M. T.; Nguyen, V.; Umrao, S.; Kim, J. H.; Tabassian, R.; Kim, J. E.; Oh, I. K. Mutually Exclusive p-Type and n-Type Hybrid Electrode of MoS2 and Graphene for Artificial Soft Touch Fingers. *Adv. Funct. Mater.* **2019**, *29*, No. 1905454.

(21) Yang, N.; Ji, X. X.; Sun, J. J.; Zhang, Y.; Xu, Q. H.; Fu, Y. J.; Li, H. G.; Qin, M. H.; Yuan, Z. W. Photonic Actuators with Predefined Shapes. *Nanoscale* **2019**, *11*, 10088−10096.

(22) Wang, Z. J.; Wang, Y.; Wang, Z. J.; He, Q. G.; Li, C. H.; Cai, S. Q. 3D Printing of Electrically Responsive PVC Gel Actuators. *ACS Appl. Mater. Interfaces* **2021**, *13*, 24164−24172.

(23) Oh, J. H.; Anas, M.; Barnes, E.; Moores, L. C.; Green, M. J. Site-Specific Selective Bending of Actuators using Radio Frequency Heating. *Adv. Eng. Mater.* **2021**, *23*, No. 2000873.
(24) Rodin, M.; Li, J.; Kuckling, D. Dually Cross-linked Single Networks: Structures and Applications. *Chem. Soc. Rev.* **2021**, *50*, 8147−8177.
(25) Zhao, T. T.; Liu, H.; Yuan, L.; Tian, X. M.; Xue, X. Y.; Li, T. K.; Yin, L. Q.; Zhang, J. H. A Multi-Responsive MXene-Based Actuator with Integrated Sensing Function. *Adv. Mater. Interfaces* **2022**, *9*, No. 2101948.
(26) Wei, L. F.; Ma, J. Z.; Ma, L.; Zhao, C. X.; Xu, M. L.; Qi, Q.; Zhang, W. B.; Zhang, L.; He, X.; Park, C. B. Computational Optimizing the Electromagnetic Wave Reflectivity of Double-Layered Polymer Nanocomposites. *Small Methods* **2022**, *6*, No. 2101510.
(27) Ma, Z. L.; Kang, S. L.; Ma, J. Z.; Shao, L.; Zhang, Y. L.; Liu, C.; Wei, A. J.; Xiang, X. L.; Wei, L. F.; Gu, J. W. Ultraflexible and Mechanically Strong Double-Layered Aramid Nanofiber-Ti3C2Tx MXene/Silver Nanowire Nanocomposite Papers for High-Performance Electromagnetic Interference Shielding. *ACS Nano* **2020**, *14*, 8368−8382.
(28) Wang, J.; Ma, X. Y.; Zhou, J. L.; Du, F. L.; Teng, C. Bioinspired, High-strength, and Flexible MXene/Aramid Fiber for Electromagnetic Interference Shielding Papers with Joule Heating Performance. *ACS Nano* **2022**, *16*, 6700−6711.
(29) Gong, S.; Sheng, X. X.; Li, X. L.; Sheng, M. J.; Wu, H.; Lu, X.; Qu, J. P. A Multifunctional Flexible Composite Film with Excellent Multi-Source Driven Thermal Management, Electromagnetic Interference Shielding, and Fire Safety Performance, Inspired by a "Brick-Mortar" Sandwich Structure. *Adv. Funct. Mater.* **2022**, No. 2200570.
(30) Wei, L. F.; Ma, J. Z.; Zhang, W. B.; Bai, S. L.; Ren, Y. N.; Zhang, L.; Wu, Y. K.; Qin, J. B. pH Triggered Hydrogen Bonding for Preparing Mechanically Strong, Electromagnetic Interference Shielding and Thermally Conductive Waterborne Polymer/Graphene@Polydopamine Composites. *Carbon* **2021**, *181*, 212−224.
(31) Zha, K. W.; Feng, C.; Han, L. P.; Li, H. R.; Yan, T. T.; Kuboon, S.; Shi, L. Y.; Zhang, D. S. Promotional Effects of Fe on Manganese Oxide Octahedral Molecular Sieves for Alkali-resistant Catalytic Reduction of NOx: XAFS and in situ DRIFTs Study. *Chem. Eng. J.* **2020**, *381*, No. 122764.
(32) Lugger, S. J. D.; Houben, S. J. A.; Foelen, Y.; Debije, M. G.; Schenning, A. P. H. J.; Mulder, D. J. Hydrogen-Bonded Supramolecular Liquid Crystal Polymers: Smart Materials with Stimuli-Responsive, Self-Healing, and Recyclable. *Chem. Rev.* **2022**, *122*, 4946−4975.
(33) Zhang, Y.; Kong, J.; Gu, J. New Generation Electromagnetic Materials: Harvesting Instead of Dissipation Solo. *Sci. Bull.* **2022**, *67*, 1413−1415.
(34) Zhang, Y.; Ma, Z.; Ruan, K.; Gu, J. Multifunctional Ti3C2Tx-(Fe3O4/Polyimide) Composite Films with Janus Structure for Outstanding Electromagnetic Interference Shielding and Superior Visual Thermal Management. *Nano Res.* **2022**, *15*, 5601−5609.
(35) Zhang, Y.; Ruan, K.; Gu, J. Flexible Sandwich-Structured Electromagnetic Interference Shielding Nanocomposite Films with Excellent Thermal Conductivities. *Small* **2021**, *17*, No. 2101951.
(36) Song, P.; Liu, B.; Qiu, H.; Shi, X.; Cao, D.; Gu, J. MXenes for Polymer Matrix Electromagnetic Interference Shielding Composites: A Review. *Compos. Commun.* **2021**, *24*, No. 100653.
(37) Zhang, W.; Pan, Z.; Ma, J.; Wei, L.; Chen, Z.; Wang, J. Degradable Cross-Linked Collagen Fiber/MXene Composite Aerogels as a High-Performing Sensitive Pressure Sensor. *ACS Sustainable Chem. Eng.* **2022**, *10*, 1408−1418.
(38) Chu, X.; Wang, R.; Zhao, H.; Kuang, M.; Yan, J.; Wang, B.; Ma, H.; Cui, M.; Zhang, X. Cross-Links−Entanglements Integrated Networks Contributing to Highly Resilient, Soft, and Self-Adhesive Elastomers with Low Hysteresis for Green Wearable Electronics. *ACS Appl. Mater. Interfaces* **2022**, *14*, 16631−16640.
(39) Guo, Y.; Zhong, M.; Fang, Z.; Wan, P.; Yu, G. A Wearable Transient Pressure Sensor Made with MXene Nanosheets for Sensitive Broad-Range Human−Machine Interfacing. *Nano Lett.* **2019**, *19*, 1143−1150.
(40) Li, M.; Chen, D.; Sun, X.; Xu, Z.; Yang, Y.; Song, Y.; Jiang, F. An Environmentally Tolerant, Highly Stable, Cellulose Nanofiber-Reinforced, Conductive Hydrogel Multifunctional Sensor. *Carbohydr. Polym.* **2022**, *284*, No. 119199.
(41) Gao, D.; Guo, S.; Zhou, Y.; Lyu, B.; Ma, J.; Zhao, P.; Pan, D.; Chen, S. Hydrophobic, Flexible Electromagnetic Interference Shielding Ffilms Derived from Hydrolysate of Waste Leather Scraps. *J. Colloid Interface Sci.* **2022**, *613*, 396−405.
(42) Zhang, D.; Yin, R.; Zheng, Y.; Li, Q.; Liu, H.; Liu, C.; Shen, C. Multifunctional MXene/CNTs Based Flexible Electronic Textile with Excellent Strain Sensing, Electromagnetic Interference Shielding and Joule Heating Performances. *Chem. Eng. J.* **2022**, *438*, No. 135587.
(43) Wu, H.; Xie, Y.; Ma, Y.; Zhang, B.; Xia, B.; Zhang, P.; Qian, W.; He, D.; Zhang, X.; Li, B.-W.; Nan, C. Aqueous MXene/Xanthan Gum Hybrid Inks for Screen-printing Electromagnetic Shielding, Joule Heater, and Piezoresistive Sensor. *Small* **2022**, *18*, No. 2107087.
(44) Guo, Y.; Zhong, M.; Fang, Z.; Wan, P.; Yu, G. A Wearable Transient Pressure Sensor Made with MXene Nanosheets for Sensitive Broad-Range Human-Machine Interfacing. *Nano Lett.* **2019**, *19*, 1143−1150.
(45) Li, T.; Zhang, J.; Jin, F.; Yang, F.; Wei, Z.; Ma, X.; Qian, L.; Sun, F.; Fan, M.; Wang, T.; Wei, D.; Feng, Z. Spontaneous Electro-Feedback Vaporesponsive Actuation Film Inspired by Mammal Hair. *Nano Energy* **2022**, *94*, No. 106933.

https://doi.org/10.1021/acssuschemeng.2c04712
ACS Sustainable Chem. Eng. 2023, 11, 5834−5844